



INSTITUT D'OPTIQUE GRADUATE SCHOOL (IOGS)

CEA-LETI, GRENOBLE
Laboratoire d'Intégration des Technologies Emissives

Report of the 3-year apprenticeship:
Integration, control and testing of innovative
photometric measuring instruments

Author:
Talla DIAGNE

Supervisors:
Eric KROEMER, CEA-LETI
Mathieu HEBERT, IOGS

July 3, 2025

Contents

Introduction	3
1 Presentation of the company	3
1.1 Gender equality at CEA	3
1.2 Emissive Technologies Integration Laboratory	3
2 What physical phenomena are behind a microLED ?	4
2.1 III-Nitrides semiconductors	4
2.2 Interband transitions	5
2.3 Influences of physical parameters	5
2.4 Specificities of a microLED	6
3 MicroLED characterization	7
3.1 Spectro-imager	7
3.2 Prober TS-3500	9
4 Motorized stage control of the spectro-imager	11
4.1 GUI design from scratch	11
4.2 Additional developed functions	12
5 Hardware validation	14
5.1 Optical Specifications	14
5.2 Measurements' specifications	16
6 Software validation	18
6.1 Luminance mapping	18
6.2 Classification of image defects	19
6.3 Autofocus functions	21
6.4 Final workflow	22
6.5 Additional functionalities	23
6.5.1 Hexagonal pixels	23
6.5.2 Stitching	24
Conclusion	24
References	26

List of Figures

1 Presentation of CEA	4
2 Illustration of a radiative interband transition	5
3 EQE as a function of current density for different LED size [8]	6

4	Picture of the spectro-imager	7
5	Understanding MTF in optical systems	8
6	Optical design of the spectro-imager	8
7	MTF simulation on the spectro-imager	8
8	Picture of a Prober TS3500 from MPI	10
9	Interface graphique pour le pilotage de la platine motorisée	12
10	Example of camera focus curve as a function of stage height	13
11	MTF measurements performed on a USAF test chart	15
12	Some methods for measuring depth of field	15
13	Spectro-imager chromaticity diagram	17
14	Zoom on measured points	17
15	Raw spectro-imager image	18
16	Processed image with software	19
17	Another map example	19
18	Example of default detection on a simulated display	20
19	Example of default detection on a real display	20
20	Another example of default detection on a real display	21
21	MTF evolution after the 3 autofocus steps	22
22	Scheme of the final workflow for the complete characterization automation	23
23	Illustration of the different hexagonal configurations	24
24	Illustration of the stitching function	24

Introduction

With the advent of optical communication technologies and virtual/augmented reality, it has been necessary to reduce the size of microdisplays to a few micrometers. At the CEA (Commissariat à l’Energie Atomique et aux Energies Alternatives) in Grenoble, new characterization methods are being implemented to characterize the microLEDs and microscreens that are manufactured. It is in this context that I am working as an apprentice-engineer within the CEA-Leti/DOPT/SNAP/LITE (Laboratory for the Integration of Emissive Technologies) on the integration of these innovative characterization methods into the laboratory’s existing ecosystem. I am working in particular on the development of software for controlling the various instruments, the acquisition and analysis of data (LIV, spectra, images, etc.).

1 Presentation of the company

Created by General Charles de Gaulle after the Second World War, CEA is an EPIC (Public Industrial and Commercial Establishment) whose objective is research and innovation. Its missions are quite cross-disciplinary and there are six main ones: energy, defense and security, digital transition, health technologies, fundamental research and remediation/dismantling. With more than 20,000 employees spread across nine centers, it is one of the largest research institutions in France. The Grenoble center is specialized in nanotechnologies, new energies, life sciences and has a worldwide reputation in the field of semiconductors. It alone employs 6,500 people, including 4,500 CEA personnel working in the center’s 115 laboratories.

1.1 Gender equality at CEA

Among the 21,763 people employed across all CEA centers in 2023, 34.8% are women. This number decreases to 27.2% in the senior manager category and 28% among engineers and researchers. However, it rises to 70.5% among administrative executives and reaches 99.2% among secretarial staff. Efforts to improve gender balance have led to 35% of new permanent hires (CDI) being women, but disparities persist in technical and managerial fields. While 40% of executive promotions were awarded to women, salary gaps remain: men earn 4.8% more among engineers and executives, whereas non-executive women earn 4.6% more than their male counterparts.

Work-life balance initiatives show progress, with more men taking part-time work (4.3%) and paternity or childcare leave (787 employees). However, part-time work remains more common among women (22.5%). Despite improvements, achieving full gender balance at CEA, particularly in leadership and technical roles, remains an ongoing challenge.

1.2 Emissive Technologies Integration Laboratory

Given its size, the CEA is divided into directorates, then institutes, departments, services, and finally multiple laboratories. The LITE lab, where I am doing my apprenticeship, falls under the Technological Research Division (DRT), more specifically the LETI Institute (Laboratory for Electronics and Information Technology). It is part of the Optics and Photonics Department (DOPT) within the New Photonics Applications Service (SNAP).



Figure 1: Presentation of CEA

The LITE lab, led by Roch Espiau De Lamaestre, focuses on microLED, OLED and LCD emitters. From design to characterization—including fabrication in cleanrooms—the lab covers highly interdisciplinary topics. My apprenticeship work falls under the characterization aspect, where I study microLED emitters. The long-term goal is to develop a color microdisplay based on gallium nitride (GaN), combining high resolution with extreme brightness. Each pixel of the microdisplay could be as small as 1 μm and individually controlled by an electronic circuit (Application-specific integrated circuit - ASIC) to produce the desired color. [1]

2 What physical phenomena are behind a microLED ?

A Light Emitting Diode (LED) is a semiconductor optoelectronic device that emits incoherent non-polarized light through electroluminescence when a forward bias is applied. The emission wavelength depends simultaneously on a few intrinsic parameters of the semiconductor material. Early LED prototypes emitted in the infrared region due to their relatively narrow bandgap (see section [2.2]), but advances in material science have progressively enabled emission in the visible spectrum—initially red, then green and blue. This last achievement, the blue LED, was realized after decades of research and was a significant breakthrough in science: its creators, Isamu Akasaki, Hiroshi Amano and Shuji Nakamura were awarded the Nobel Prize in Physics in 2014 for their work.

Improvements in design and materials have also significantly increased the luminous efficacy, making LEDs highly efficient light sources in modern applications. At LITE, our work on LEDs focus on III-Nitrides, mainly for microdisplays intended for virtual and augmented reality

2.1 III-Nitrides semiconductors

Nitride materials are III-V semiconductor compounds in which nitrogen serves as the group V element. Common examples include gallium nitride (GaN), indium nitride (InN), aluminum nitride (AlN), and their ternary alloys such as InGaN. These materials are characterized by their tunability, combined with their high internal quantum efficiency, which makes them particularly well-suited for optoelectronic applications. Among these, nitride-based LEDs have become the foundation of modern solid-state lighting, enabling significant improvements in energy efficiency and durability, and driving a global transformation in lighting technologies over the past few decades. [2]

2.2 Interband transitions

In semiconductors, electrons occupy two main energy bands: the conduction band (CB) and the valence band (VB). At absolute zero, the VB is fully occupied, while the CB is empty. An electron can be excited from the VB to the CB if it absorbs an energy greater than the bandgap energy E_g , which separates the two bands — this is known as the photoelectric effect. When the electron relaxes back from the CB to the VB, it releases energy in two possible forms: as heat, through phonon emission, or as light, via photon emission. If this process is triggered by an injected electron, it is called electroluminescence; if it results from photon absorption, it is referred to as photoluminescence.

Materials used for LED application in optoelectronics are typically direct bandgap semiconductors, where the minimum of the CB and the maximum of the VB occur at the same wave vector \vec{k} in the first Brillouin zone. This explains why, in the first LED patent, the use of silicon carbide (SiC), an indirect bandgap material, resulted in very low efficiency — no more than 0.03 % at 430 nm. In indirect semiconductors, since the CB minimum and VB maximum are not aligned in \vec{k} -space, interband transitions require the assistance of phonons or crystal defects to conserve both energy and momentum, as photons alone cannot provide the necessary change in wave vector. Consequently, not all of the energy from de-excitation is converted into light: a significant portion is lost as heat, making the process slower and less efficient. This is why direct bandgap semiconductors are favored for light emission.

To enhance radiative recombinations, heterojunctions are commonly used. In such structures, the active region is made of a material with a lower bandgap energy compared to the surrounding layers. This creates a potential well that confines both electrons and holes. When the thickness of this region is reduced to just a few nanometers, discrete energy levels appear — this structure is known as a quantum well. [3]

2.3 Influences of physical parameters

My apprenticeship work focuses on nitride-based microLEDs. These materials can emit light across a broad spectral range, from ultraviolet (UV) to infrared (IR). Despite their favorable bandgap characteristics, the emission spectrum of nitride microLEDs can be relatively broad. This is mainly due to the random incorporation of indium during the growth process, which leads to potential fluctuations at the microscopic level. Nevertheless, nitrides can still achieve very high internal quantum efficiency (IQE, see Formula [1]), even in the presence of significant defect densities, such as threading dislocations. Additionally, the use of InGaN underlayers is essential for the growth of high-quality quantum wells (QWs). An underlayer is a thin layer of material placed below the main layers of a semiconductor structure. In this case, the InGaN underlayer helps by reducing lattice mismatch between the substrate and the subsequent layers. This reduction leads to less defects.

Another consequence of using InGaN QWs is the appearance of an internal electric field within the well. This internal field originates from polarization effects, which typically include two components: a spontaneous polarization term P_{sp} which is intrinsic to the material, and a piezoelectric polarization term P_{pz} which arises from the mechanical strain due to the lattice mismatch when InGaN is grown on GaN. [4] However, since the spontaneous polarization values of GaN and InGaN

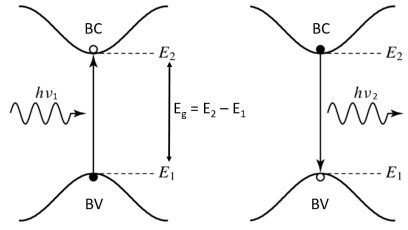


Figure 2: Illustration of a radiative interband transition

are approximately equal ($P_{sp}(\text{GaN}) \approx P_{sp}(\text{InGaN})$), the resulting potential difference (and thus the internal electric field) is mainly caused by the piezoelectric component. This polarization causes the apparition of an internal electric field, which slows down the radiative recombination processes and results in an IQE peak at lower current densities. Despite this shift, the maximum IQE value remains constant, in agreement with the ABC model:

$$IQE = \frac{b \cdot In^2}{a \cdot In + b \cdot In^2 + c \cdot In^3} = \frac{\text{number of photons emitted from the active region}}{\text{number of electrons injected into the LED}} \quad (1)$$

$$J \propto a \cdot In + b \cdot In^2 + c \cdot In^3 \quad (2)$$

For the sake of completeness, we can recall that $A = a \cdot I$, $B = b \cdot I$ and $C = c \cdot I$ are the coefficients for respectively: the Shockley–Read–Hall (SRH) recombination, the radiative recombination, the Auger recombination [5]. This model assumes that carrier densities n (electrons) and p (holes) are equal.

2.4 Specificities of a microLED

From the beginning of the 2000s already, Choi et al. already showed that microLEDs have a better light emission than macrometric-sized LEDs [6], which shows that it's really not a very recent subject. This size-dependent performance arises from several physical mechanisms. While macroscopic LEDs suffer from current crowding and efficiency droop at high injection levels, microLEDs benefit from improved current spreading and enhanced thermal dissipation. However, microLEDs also introduce new challenges that must be considered in device design and fabrication.

Additionally, when working with microLEDs, it is important to note that increasing the quantum well (QW) thickness can also lead to longer diffusion lengths, which may result in an efficiency loss, possibly due to non-radiative SRH recombinations occurring at the sidewalls. [7]

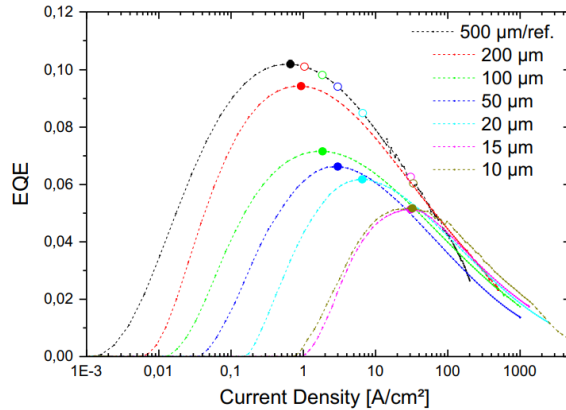


Figure 3: EQE as a function of current density for different LED size [8]

3 MicroLED characterization

Developing microdisplay technologies using μ LED or OLED on ASIC platforms requires precise measurement solutions. We need to capture the luminance of each pixel on a probe test station to identify defective pixels, to measure luminance variability and to adjust pixel luminance through a control ASIC. This development followed the European Hilico project, which focused on creating a GaN microdisplay on an ASIC with $10\text{ }\mu\text{m}$ pixels.

Previous methods for analyzing microdisplay pixels had limitations. Spectrophotometers measured overall luminance but not individual pixels. High-resolution cameras provided quick overviews but lacked detail on defective pixels or luminance variability. Using probe stations to reconstruct images through stitching was time-consuming and complex, and it did not provide luminance data for individual pixels. These challenges highlight the need for a more efficient solution for pixel-level luminance analysis in microdisplay technologies.

3.1 Spectro-imager

A spectro-imager is an optical instrument designed for both imaging and spectroscopy. This tool is essential for creating luminance maps of microLEDs integrated on ASICs.

The system features a complex optical design with more than 12 lenses (Figure[6]). It is capable of imaging objects as small as $2.5\text{ }\mu\text{m}$ across a total field of view measuring $8 \times 6\text{ mm}^2$ with a magnification of $\times 4.5$. For spectroscopic measurements, the instrument can achieve a spectral resolution down to 2 nm across the visible range. In 2022, a bid was launched to equip the DOPT with the capability to measure all the pixels of a microdisplay on an ASIC with these specifications. Several potential suppliers offering commercial solutions were identified but none met the expected requirements. The first tender was unsuccessful, leading to the launch of a second one. Only ELDIM was able to respond to this tender by proposing to adapt a previous version of their products to meet most of our specifications. However, per-pixel colorimetry was not achievable, and the working distance was reduced from 20 mm to 17 mm.

Developing the device was filled with challenges. Initially, the goal was to achieve an MTF (Modulation Transfer Function) exceeding 30% for a 500 lp/mm pattern. MTF is a measure of how well an optical system can reproduce the details of an object -i.e frequencies higher and higher-, expressed as a percentage. The lp/mm unit stands for line pairs per millimeter, used to describe the resolution of an optical system and indicating how many pairs of black and white lines it has within one millimeter. Achieving a high MTF at such a fine resolution was crucial for ensuring the device could accurately capture and analyze increasingly small microLEDs.

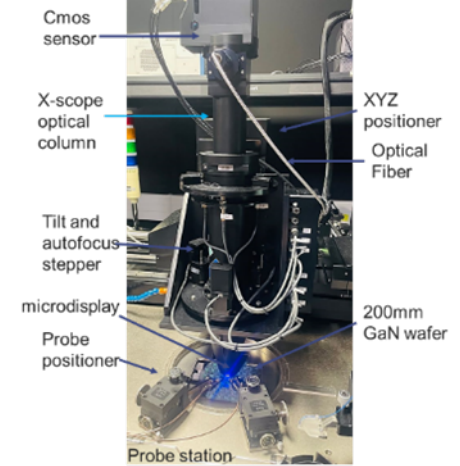


Figure 4: Picture of the spectro-imager

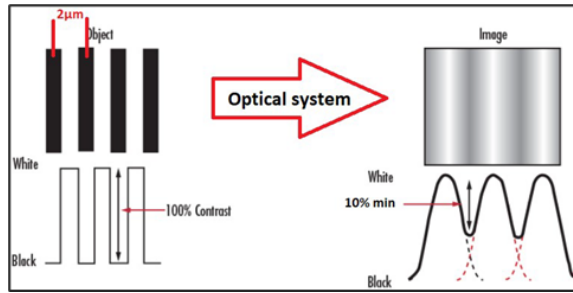


Figure 5: Understanding MTF in optical systems

However, the first version of the spectro-imager did not perform well as shown in Figure [7], prompting a complete redesign and reassembly by ELDIM. To enhance performance, the optics were carefully chosen, and a new tolerance analysis was conducted using ZEMAX optical simulations. Assembly processes were upgraded with a new machine that automates the alignment of optics with precision better than 5 micrometers, a task previously done manually by technicians.

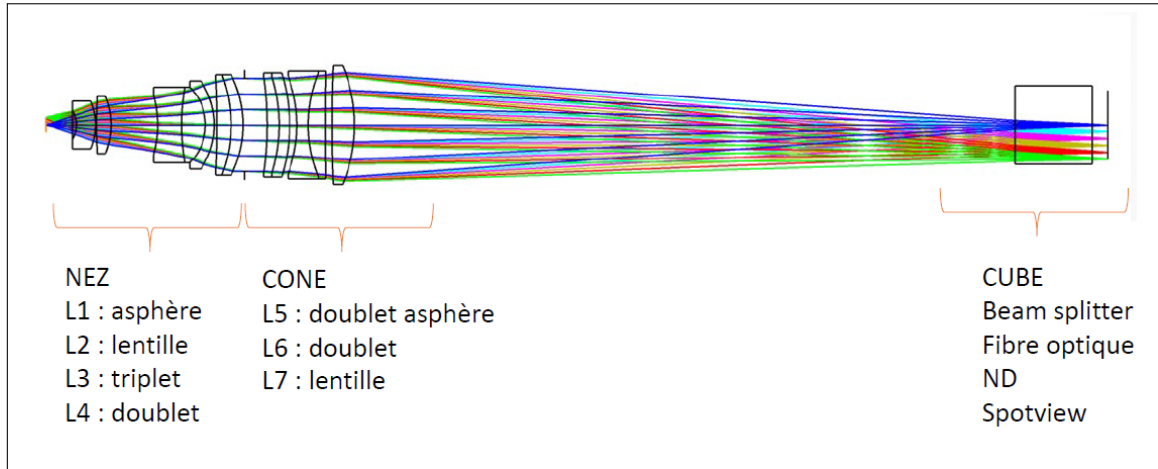


Figure 6: Optical design of the spectro-imager

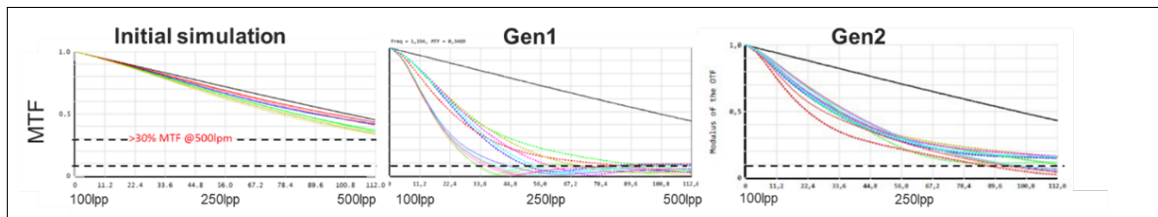


Figure 7: MTF simulation on the spectro-imager

The system also includes software for automated microdisplay analysis: uniformity, resolution, contrast, defects, flicker. The goal is to control all these functions with Python to centralize them with all other Python codes already used in the lab for operating the characterization workflow. This will allow us to automatize wafer characterization, from measurement to analysis of the obtained data. However, even the software controlling the device was initially inadequate and required significant improvements and many updates -*still in progress*- before the hardware could be approved.

To facilitate transitions between different imaging modes, the spectro-imager is integrated with motorized stages. This setup is crucial for enhancing the efficiency and precision of the measurements. To easily switch between the microscope and spectro-imager, these instruments are mounted on motorized stages. The section [4] focuses on controlling this motorized support.

3.2 Prober TS-3500

The test bench also has a key component known as the MPI TS-3500 Prober system. A wafer prober is a piece of equipment used in the semiconductor industry to test the electrical characteristics of circuits on semiconductor wafers. It allows the precise placement of probes on the tiny contact pads of integrated circuits or microLEDs on a wafer, which is essential for verifying the functionality and performance of each device before the wafer is cut into individual chips.

This particular prober system is equipped with micropositioner-controlled probes (micropositioners) that offer sub-micrometer positioning accuracy. Such precision is crucial for accurately contacting the pads, which are the metallic contact areas of the microLED representing the anode and cathode. These contacts are allow us to establish electrical connections and turn on the μ LEDs.

In the image below [8], we can see a photo of the prober, which is equipped with two touch screens for control. These screens allow us to navigate the map of the wafer being studied, making it easy to move to different areas on the wafer. Additionally, you can use these screens to automatically focus the microscope -when used-, ensuring precise placement of probes on the microLED contact pads. There are also two red emergency stop button visible on the prober. When studying a wafer, the prober creates a vacuum on the wafer to hold it securely in place, providing stability and accuracy in measurements.



Figure 8: Picture of a Prober TS3500 from MPI

The emitted light intensity depends directly on the current through the microLED, which itself varies with the applied voltage across the pads. For macroscopic LEDs, the Shockley diode equation accurately describes this relationship:

$$I = I_S \left(\exp \left(\frac{eV}{kT} \right) - 1 \right)$$

where the saturation current I_S is given by:

$$I_S = eA \left(\sqrt{\frac{D_p}{\tau_p}} \frac{n_i^2}{N_D} + \sqrt{\frac{D_n}{\tau_n}} \frac{n_i^2}{N_A} \right)$$

Here, A represents the cross-sectional area of the PN junction, n_i the intrinsic carrier density, N_A and N_D respectively the acceptor and donor doping concentrations, τ_n and τ_p the electron and hole lifetimes, D_n and D_p the corresponding diffusion coefficients, k the Boltzmann constant, T the temperature, and e the elementary charge. However, this model fails to accurately describe microLED behavior as it doesn't account for microscale specific effects. To address this limitation, we use empirical characterization methods at LITE. The data from these functions allow us to access two key curves: $I = f(V)$ (current-voltage) and $L = f(V)$ (luminance-voltage), commonly referred to as IVL characteristics when superimposed.

The prober enables automated sequential measurements across all wafers in a given batch - we call such a prober a *full automatic* one. All pLED electrical characterization is already automated in a Python environment that already exists in the lab, result of several years of development. A National Instruments software platform controls the voltage/current input to the microLEDs. The system also integrates the spectro-imager from ELDIM previously described and an alignment microscope. Both are connected via an optical bridge for an easier way to switch between imaging

modes. The microscope facilitates probe positioning and microLED activation, while the spectro-imager provides spectral characterization.

4 Motorized stage control of the spectro-imager

Chronologically, this part was developed before the spectro-imager arrival. As explained in the previous section, due to a lot of problems faced during the conception of the spectro-imager, its delivery date was repeatedly delayed. So before its arrival I got ahead in my work and had to design an intuitive graphical user interface (GUI) to control the stage movements with micrometer precision. It was also necessary to ensure it would be impossible to move it too far or too low, to prevent damage to either the spectro-imager or surrounding equipment.

4.1 GUI design from scratch

The software I used to design the graphical interface is called *Qt Designer*. We can then implement these interfaces in Python code, assigning specific functions to each button:

```
1 from PyQt5 import uic, QtWidgets
2 import pyqtgraph as pq
3 qtcreator_file = "file_path.ui"
4 Ui_MainWindow, QtBaseClass = uic.loadUiType(qtcreator_file)
5 uiclass, baseclass = pq.Qt.loadUiType(qtcreator_file)
```

First, I had to develop the low-level function library to send basic commands to the motor and read its responses. This was perhaps the most complex part, as the commands were written in SCL (Structured Control Language). Higher-level functions were then implemented to send more complex commands: move a specific distance along a given axis, go to a particular position, locate limit sensors, etc. The travel distance is communicated to the motor in units of *counts*, where each count's value depends on the motor resolution. The interface is shown in Figure [9].

Upon launch, all buttons are disabled except for *Initialization*, which appears in red. This button activates the connection with the motorized stage and initializes it. First, it sets movement limits for all three axes. Then, for each axis, it moves and locates all six limit sensors. Finally, it positions the stage at mid-point for X and Y axes and at the top for Z axis. I chose this method as a safety prevention, in order to avoid an accident by accidentally going too low. The *Move to reference position* button allows returning to this initial configuration. Users can adjust the motor movement speed and set the Z-axis limit to prevent camera damage.

The interface offers two modes (millimeters/micrometers) with adjustable *Jog* step size for precise movements along all axes. The program continuously monitors step values and disables buttons if movement would exceed limits. This function should however be disabled if one looks for a less time-consuming software, but if not, it's safer to let it as it. The right section allows absolute positioning by entering XYZ coordinates and clicking *Go to XYZ coordinates*. The bottom section includes a text console for user communication and displays the real-time motor position. Upon closing, the software prompts the user to reset motor positions before shutdown.

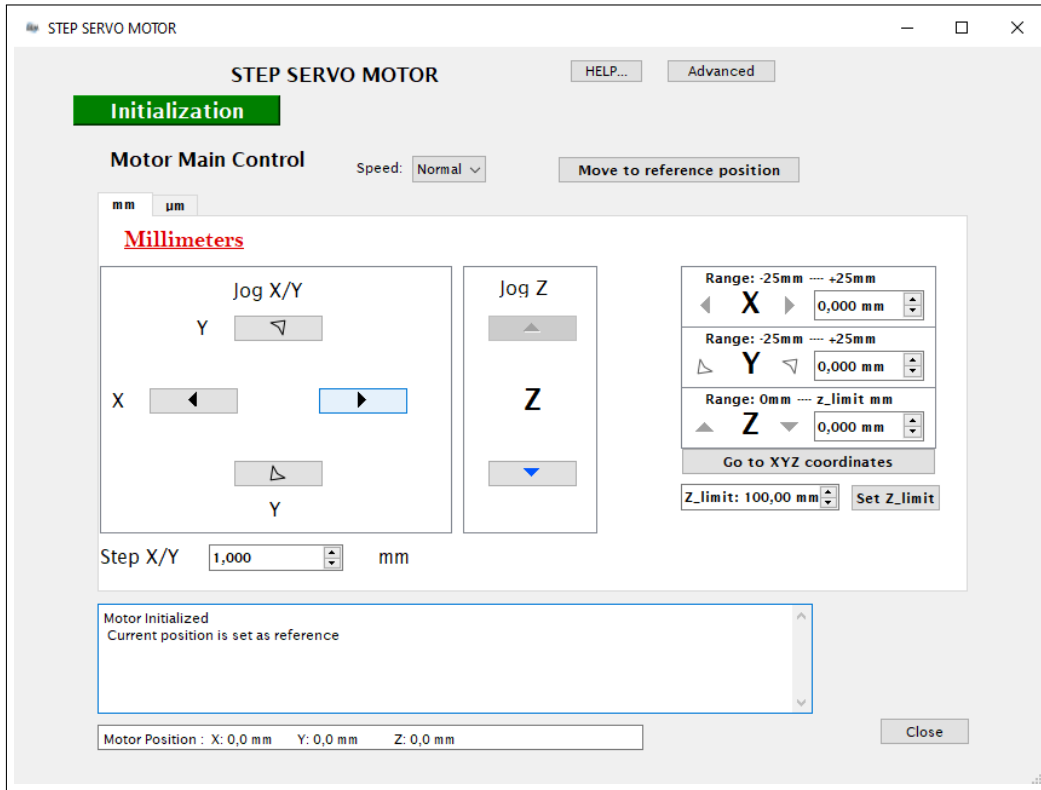


Figure 9: Interface graphique pour le pilotage de la platine motorisée

4.2 Additional developed functions

- **Autofocus Function:** A simple way to verify the proper functioning of my control functions is to associate them with a homemade autofocus function. This function automates the focusing process of a camera by adjusting its position along the vertical axis, capturing images, and analyzing their focus quality. It begins by defining the necessary variables, such as the axis, limit positions, and step size. The function then enters a loop where the camera is moved in successive steps: at each step, the current position is read, and a focus score is calculated and attributed to that position. The focus score is computed as follows: each captured image is first converted to grayscale, then a Laplacian is applied through convolution using one of the two following kernels, which yield the same result:

$$\begin{pmatrix} -1 & -1 & -1 \\ -1 & 8 & -1 \\ -1 & -1 & -1 \end{pmatrix} \quad \begin{pmatrix} 0 & -1 & 0 \\ -1 & 4 & -1 \\ 0 & -1 & 0 \end{pmatrix}$$

The score then corresponds to the variance of the resulting output image: for a sharp image, the intensity variations are abrupt, and its Laplacian (i.e., the second derivative: $\Delta f = \nabla^2 f = \nabla \cdot \nabla f$) consequently highlights the image edges more distinctly - resulting in high variance.

The focus positions and their corresponding scores are recorded. If the current score exceeds the best recorded score, both this score and its corresponding position are updated. The loop is stopped when the position exceeds the end position. Once the optimal focus position is found, the camera moves to this position. A graph is generated to visualize the focus scores as a function of camera positions: Figure [10] shows the optimal focus position corresponding to the curve's maximum. The function also handles exceptions by capturing any errors occurring during execution and displaying them in the user interface or raising them for subsequent processing.

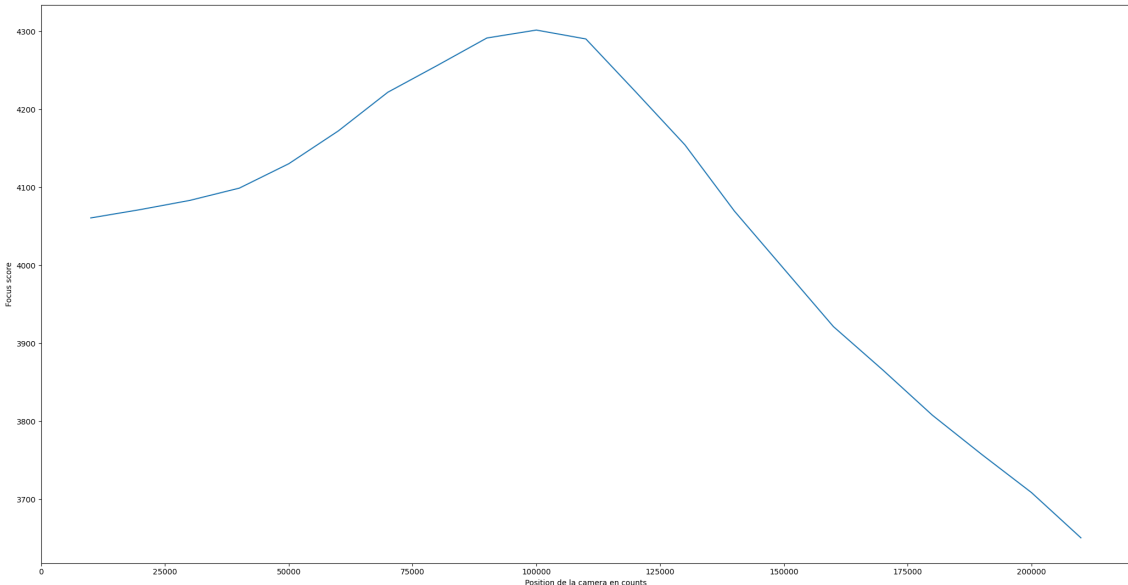


Figure 10: Example of camera focus curve as a function of stage height

A potential optimization for this function would be: in cases where we're certain the best focus lies within the given position range, we could interrupt the function as soon as the curve starts descending. This would approximately halve the processing time. It's also necessary to determine the camera's optimal exposure time as this represents a significant time-limiting factor here.

I also propose the following alternative method to test for performing the same task:

- By calculating the mean frequencies of the image's Fourier transform: a sharp image contains more details and therefore higher frequencies

5 Hardware validation

During the bidding for the spectro-imager, a detailed specification was established to ensure the device's compliance with the expected performance and quality requirements. This section presents these criteria (already mentionned in section [3.1]) as well as the tests and validations carried out to verify that the spectro-imager meets these requirements. A green dot indicates that the specification is validated, a red dot signals a specification that is not met, and a black dot designates tests that have not yet been carried out at the time of writing this report.

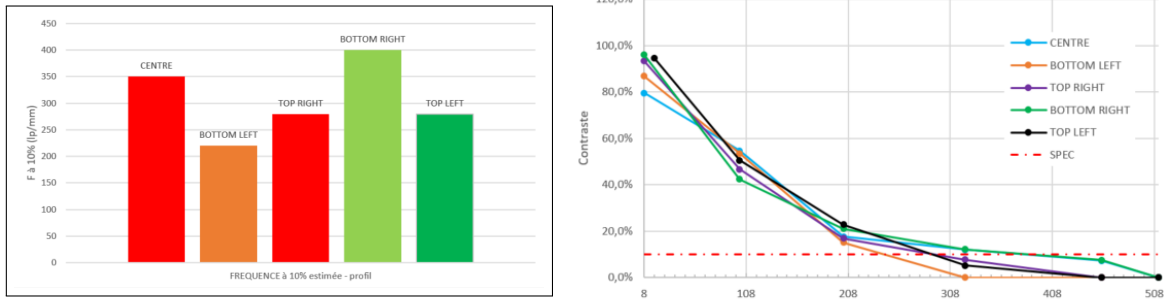
Many of the experiments to check these specifications have not been carried out yet. Instead, I tried to focus on the most important ones and the automation of the software. The main goal was to have a working workflow characterization process and due to the very late delivery of the spectro-imager, I had to choose wisely which specifications really needed to be checked first. However, I still tried to mention a few experiments that could be helpful to verify them.

5.1 Optical Specifications

- Optical field: at least $8 \times 5 \text{ mm} \Rightarrow 8 \times 6 \text{ mm}$. This allows imaging a full microdisplay in a single capture, significantly enhancing workflow efficiency and reducing characterization time.
- Size of the smallest measurable component: $2 \mu\text{m} \Rightarrow$ Smallest measured dimension: $2.5 \mu\text{m}$. This specification is a direct consequence of the MTF value measured in the next point.
- Resolution of the optical system: 10% for a frequency of approximately 500 line pairs/mm \Rightarrow measured at approximately 300 line pairs/mm

This test was done by imaging an USAF target illuminated by a lightsource. After opening the images with ImageJ/Fiji software, the contrast is manually calculated using two methods: by tracing the profile and with the histogram. The frequency estimated at 10% is then averaged over the two methods. However, overall, the method using the histogram gives much higher and thus less realistic results. This is maybe due to the fact that it includes all pixels, even those from very bright or dark areas that aren't representative.

The same measurement is performed at 5 different locations on the screen: at the center, top left, top right, and similarly at the bottom. These measurements then allowed plotting the MTF graphs below (Figure [11]). The different values of MTF obtained at these locations (175 line pairs/mm between the minimum and maximum) can have two origins in my opinion : it's either due to a bad performance of the focus process or to aberrations within the camera. The maximum values, however, remain well below the required value.



(a) Spatial frequency at 10% contrast as a function of position in the field (profile method)

(b) Average MTF (profile method)

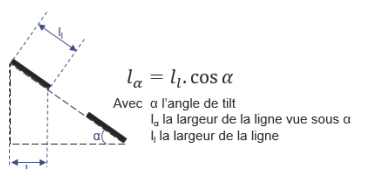
Figure 11: MTF measurements performed on a USAF test chart

- Detection of a dead pixel: the measured luminance of a dead pixel in the middle of 8 lit pixels must be less than or equal to 10% of that of the surrounding pixels \Rightarrow
Since it is still difficult to control such small pixels, the simplest method would be to design a mask with a 3×3 microLED pattern with the center one not emitting light.
- Working distance: greater than 20 mm \Rightarrow measured at 17 mm; although the specification is not met, the space is sufficient to place the micropositioners. A compromise was found by validating this specification.
- Depth of field: Essential: greater than or equal to $3 \mu\text{m}$. Desirable: greater than or equal to $8 \mu\text{m}$

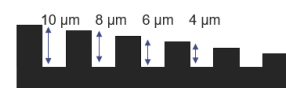
Several options are available to us here to verify the depth of field value. It is possible to purchase commercial depth of field measurement test charts (Figure 12a). Another possibility would be to use the Ronchi rulings already at our disposal. The latter have patterns of line pairs at a given frequency (between 50 and 500 line pairs/mm), and by tilting them, we could determine over what height the line pairs are still sharp (Figure 12b). We could also fabricate a test chart with "pixels" of different heights. The depth of field would correspond to the maximum height for which, by focusing on the upper part, the background remains sharp (Figure 12c).



(a) Example of a test chart from Edmund Optics



(b) Tilted Ronchi ruling



(c) Test chart with different depths

Figure 12: Some methods for measuring depth of field

5.2 Measurements' specifications

- **Luminance:** 5×10^{-3} to 10^6 cd/m^2 with accuracy better than $\pm 3\% \Rightarrow$

The minimum value is the simplest to verify here. The spectro-imager comes with three optical densities (OD0, OD2, and OD4). We also have calibrated light sources with known luminance values at specific supply voltages. The procedure is to use the strongest density (OD4, which provides a $10^4 \times$ attenuation) on a source emitting approximately 50 cd/m^2 . For the maximum value, the LITE lab fabricates microLED sources reaching up to 10^6 cd/m^2 .

To study luminance homogeneity across the camera's field, we can mask a light source (e.g., a backlight) with a sufficiently small aperture, then take multiple measurements while moving the source-mask assembly (not just the mask, to avoid spatial inhomogeneity artifacts). This ensures each measurement goes to a different camera region. Comparing these values allows a verification of field uniformity.

For luminance measurement precision, repeated measurements at the same position are sufficient.

- **Colorimetry:** Accuracy of at least 0.003 on chromaticity coordinates $(x, y) \Rightarrow$

Verification method: Using a calibrated source, I performed successive measurements and analyze the standard deviation of the obtained chromaticity coordinates. Tests cover multiple colors (white, red, green, blue) to ensure uniformity. We use an Effilux backlight with $>90\%$ homogeneity; thus, source movement between measurements should be avoided. I also contacted Effilux to request the calibrated spectral curves of the lamps. This allowed me to compare them with the curves obtained using the spectro-imager. It is recommended to pre-verify the luminance stability using a luminance meter. Another suggestion is to study the aging of the Effilux lamps used to calibrate the spectro-imager. The precision of my measurements could be significantly improved by taking many more data points. I only took 5 measurement points for each color.

After imaging the backlight with the spectro-imager, the ELDIM software gives us back the colorimetric coordinates of the backlight's colors. I also wrote a Python code that takes as an argument the spectral curve and also calculates these coordinates in order to check their reliability by comparison with the coordinates given by the ELDIM software. The code can also plot these color values on a chromaticity diagram, which visually represents the range of colors detectable by the human eye. It calculates color purity, indicating how close a color is to being purely spectral. Additionally, the code computes statistical values like mean and standard deviation for various sets of color data.

Table [1] summarizes results from 5 measurements per backlight. For each color, I calculated the deviation of each measurement from the mean measured and took the max deviation obtained. I chose this method because, as explained above, the measurement sample is too small and calculating the standard deviation could be irrelevant. The achieved precision far exceeds the 0.003 requirement ($100 \times$ better). Figure [13] shows excitation purity near 100% for red/blue, with wavelength accuracy within 5–10 nm. This will be further analyzed via spectroscopic resolution tests.

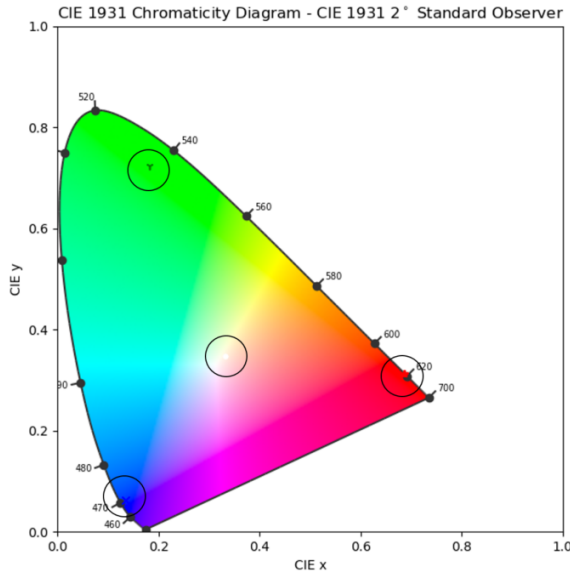
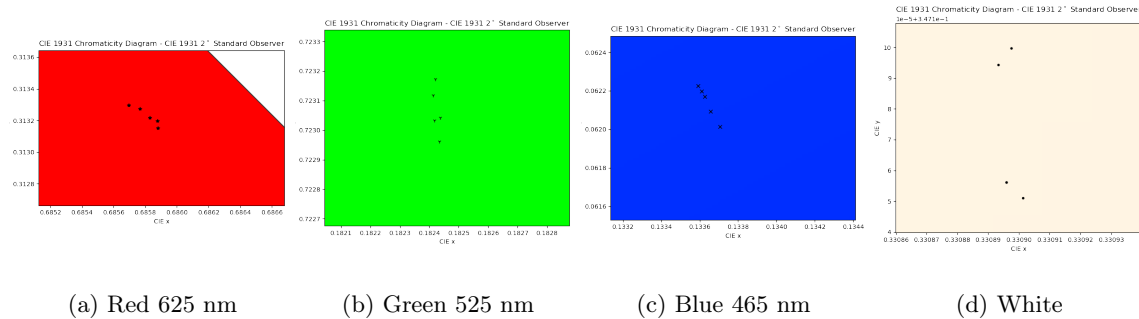


Figure 13: Spectro-imager chromaticity diagram



(a) Red 625 nm

(b) Green 525 nm

(c) Blue 465 nm

(d) White

Figure 14: Zoom on measured points

Color	Max deviation (x)	Std (x)	Max deviation (y)	Std (y)
White	0.438	4.936×10^{-5}	0.432	$7,094 \times 10^{-5}$
Green	0.208	$3,193 \times 10^{-5}$	0.697	$3,369 \times 10^{-5}$
Red	0.688	$7,396 \times 10^{-4}$	0.312	$7,736 \times 10^{-4}$
Blue	0.130	$1,130 \times 10^{-4}$	0.083	$1,922 \times 10^{-4}$

Table 1: Max deviation of (x, y) coordinates for each color

- **Spectroscopy:** 2 nm spectral precision between 400–800 nm ⇒ Spectral range: 380–720 nm (limited to visible light, so because we work on LEDs we can

validate this criterion). For resolution verification, a mercury vapor lamp (with sharp and well-defined emission lines) is measured repeatedly to assess spectrometer repeatability and precision.

6 Software validation

As explained previously, many updates were necessary to achieve a functional software. At the time of writing, more updates are still expected in order to repair bugs. However, the main tasks are now doable with the soft, and in this section, I will present some of the beautiful results we obtained with the spectro-imager.

6.1 Luminance mapping

This figure [15] presents sample images from microLED arrays from a project the lab is currently working on. The display is made of 330×185 microLEDs array ($10 \mu\text{m}/\text{pixel}$) displaying a spaceship and the CEA's logo:



Figure 15: Raw spectro-imager image

In figure [16], each pixel represents a microLED with 12-bit intensity scaling (0–4095). The software automatically crops screen edges (creating a "map"). This map is a 330×185 pixels image, instead of 7920×6004 in the original image [15]. Each pixel on this map corresponds to a single microLED from the original image. The mapping process also measures a central 1 mm diameter region for per-pixel luminance calibration. Thanks to this, each pixel value on the maps gives us the luminance of the corresponding microLED imaged.

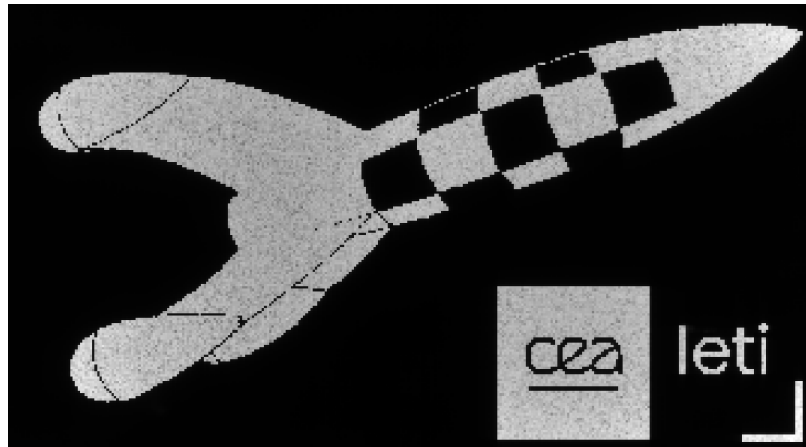


Figure 16: Processed image with software

Figure [17] reveals macroscopic defects (likely fabrication-related) in a fully lit array. With such images for example, the spectro-imager can provide valuable feedbacks to the design and process teams of the lab.

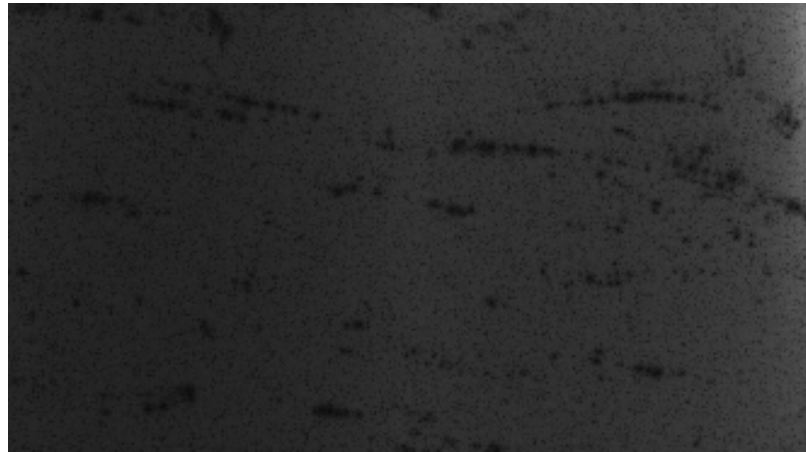


Figure 17: Another map example

6.2 Classification of image defects

The software is able to detect different kinds of microdisplay defects: Luminance disparities, dead lines/columns, round corners, black spots, ASO (abnormally switch on), horizontal/vertical bands, scratches. In order to test this feature of the software, I had to code a function using Python in order to simulate microdisplays with very specific defects. In the figure below, a display is simulated with one defective line and column, and 5 clusters. I had to simulate this because at that time, the spectro-imager was still not delivered so I had to figure out a way to test the software in the meantime.

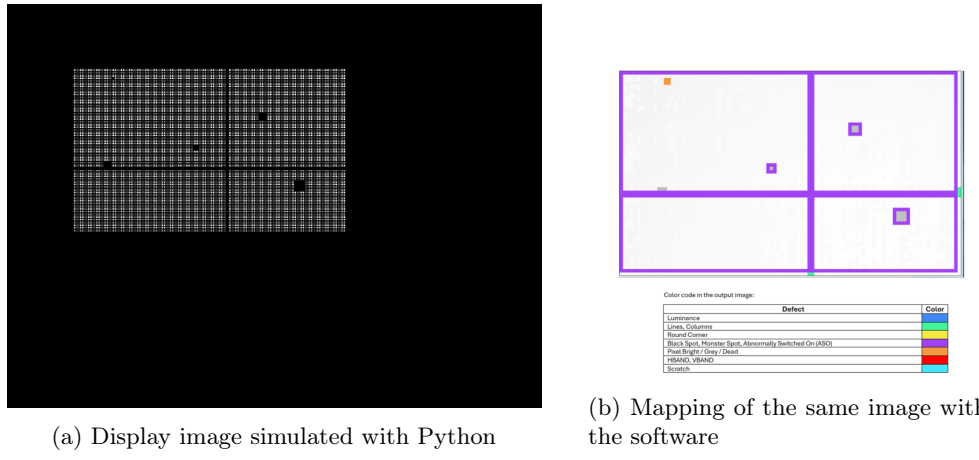


Figure 18: Example of default detection on a simulated display

Once the spectro-imager was available, I was able to capture real images of microdisplays. In the following figure [19], one can observe some luminance defects that have been outlined in purple. These defects were identified as black spots according to [18b].



Figure 19: Example of default detection on a real display

In the figure below, there are significantly more defects detected. However, the outlining is less precise because this function need us to coordinate seven different parameters, which can be challenging. This could be a very useful direction for future work : to find an algorithm that optimizes the seven parameters at the same time.



Figure 20: Another example of default detection on a real display

Below is a list of the seven parameters in question that must be adjusted simultaneously to optimize defect detection:

- ThresholdPercentage: defines the percentage threshold above which a row/column is considered defective
- LowThresholdRatio: defines the threshold below which a pixel is considered potentially "dead." If several neighboring pixels are detected, a black spot is identified
- HighThresholdValue: defines the maximum value above which a pixel can be considered "bright." If several neighboring pixels are detected, they are considered a black spot
- ThresholdRatio: defines the limit above which a pixel is considered Abnormally Switch On (lit)
- KernelSize: defines the size of the area used around each pixel for the process
- DeviationTolerance: defines the maximum allowed deviation for dark pixel values
- DeviationToleranceBright: defines the maximum allowed deviation for bright pixel values

6.3 Autofocus functions

In this part, the main goal was to test how accurate were the different autofocus functions of the spectro-imager. This includes the large and close autofocus, and then the tilt regulation. The 3 steps correspond respectively to: a rough adjustment, a fine adjustment, and tilt adjustment controlled by 3 stepper motors. These different functions are executed from XML recipes located in a given folder. Before executing the movements, the motor pause is set to 100 ms instead of 1500 ms to speed up the characterization process.

I then developed a Python code designed to analyze an image by dividing it into a grid of segments and calculating the MTF for each sub-image. It uses several libraries including matplotlib for visualization, numpy for numerical operations, and PIL for image processing. The main class, *fijicontrol*, contains three functions. The *open* method is the primary function that reads an image, divides it into an $n \times n$ grid, and processes each segment. It starts by loading the image and determining its dimensions. The image is then split into smaller segments based on the specified grid size. For each segment, the method crops the image and calculates the MTF value using the *verif freq* method. The MTF values are stored in a matrix for later use. The *crop* method helps in extracting a specific region from the image based on the provided coordinates and dimensions.

The *verifreq* method computes the MTF for a given image segment by projecting the image along the vertical axis and calculating the contrast ratio. If the maximum and minimum values of the projection are equal, the method returns zero, indicating no contrast variation. Otherwise, it returns the normalized MTF value. After processing all segments, the *open* method visualizes the results by overlaying a color-coded grid on the original image. Each segment is colored according to its MTF value, with a colorbar indicating the scale. The final visualization is saved as a PNG file with a high resolution.

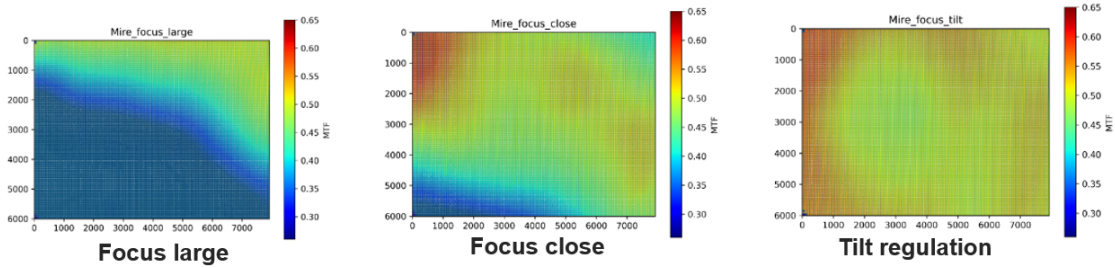


Figure 21: MTF evolution after the 3 autofocus steps

The image above shows the results from three steps of the autofocus process, and we can see it gets better at each step. First, in the Focus Large step, the focus is wide and the image is not very sharp. Then, in the Focus Close step, the focus gets narrower and the image becomes clearer. Finally, in the Tilt Regulation step the focus is fine-tuned and the image is the sharpest. Between the close and tilt steps, the MTF becomes more uniform, which means it worked well.

6.4 Final workflow

In this section, I had to combine all the functions I developed in order to activate all the characterization workflow from just one control. This was the ultimate goal of my 3-year apprenticeship.

The process begins with the positioning of the support (should be done only once), followed by the initialization phase explained in [4.1]. The user must then launch ELDIM's CameraLiveView in order to help him position themselves **approximately** around the focus position, and then move slightly below this position. This is because the first step of the autofocus process (i.e the Focus Large) works by looking step by step upward. This is done to avoid any accident with the device under test (DUT).

The automation of the ELDIM software is then activated via the *main.py* script, which takes as input the file name, the address of a folder, the number of display pixels, and the hexagonal configuration. This process takes 32 seconds, plus approximately 5 minutes for the three focus adjustments. It launches multiple processes simultaneously in the background. The initialization checks if STXCom is running (and launches it if not) before configuring the SOAP connection. SOAP, for Simple Object Access Protocol, is a protocol used for exchanging structured information in web services. In this case, it's used to communicate with functions developed by ELDIM. The measurement preparation positions the motor at mid-course (2500 μm), writes all the focus recipes in a XML format, and performs autofocus (with large/close/tilt adjustments if needed). The acquisition launches the measurement via XML recipes, captures the image and its black

reference. The processing creates a map of pixels with their luminance values, calculates the mean and standard deviation, identifies defects, and classifies them using a color code. The spectral curve is also saved, with the colorimetric coordinates measured from it. This file is also used to be combined with the raw image in order to have access to the absolute scale that allows us to go from the 12 bits to the actual luminance measured. Finally, the results are recorded with marked defects and the buffers are cleaned.

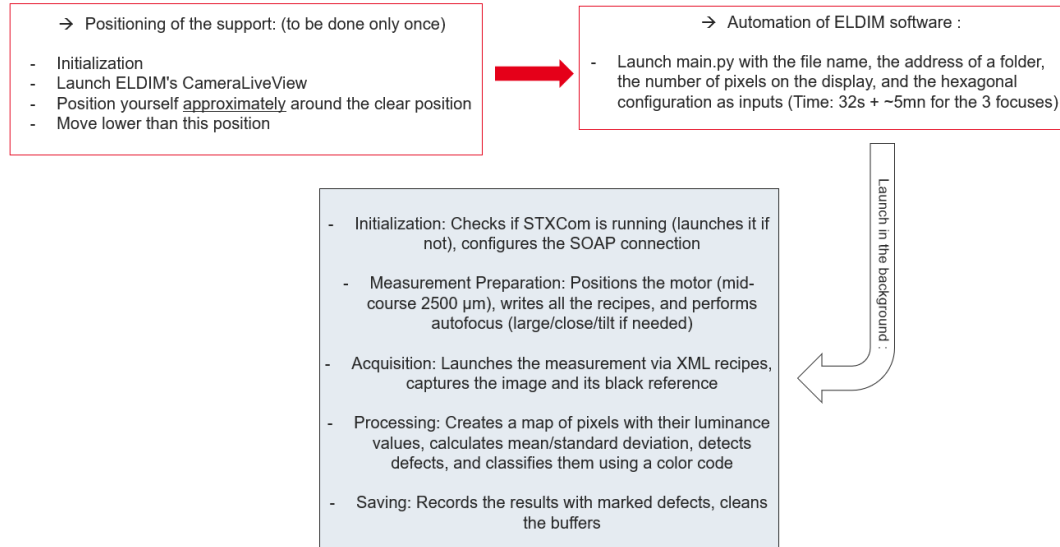


Figure 22: Scheme of the final workflow for the complete characterization automation

6.5 Additional functionalities

These additional functions were added after the initial delivery of the spectro-imager to enhance its capabilities and adaptability for more complex images. Since they are very new and updates are still expected, I didn't have much time to work on them. However, I already implemented one of them in my workflow process but I still lack a total understanding on how they fully work.

6.5.1 Hexagonal pixels

The use of hexagonal pixels will be very useful within the next years, especially for optical fiber applications in datacom/chip-to-chip communication. The main goal of these masks is to match the pattern of optical fibers, which helps the system to capture and to process data accurately, improving communication performance. The spaces between hexagonal pixels are important because they prevent crosstalk, ensuring each pixel's data is clear and reducing interference.

An update in ELDIM's software enables it to deal with hexagonal pixel arrangements. The image below shows an important part of this feature: the hexagonal configuration. I already introduced this new parameter in the Python code I developed.

1 : 1 pixel allumé sur 4 :		
2 : 2 pixels allumés sur 4 :		
3 : 3 pixels allumés sur 4		
4 : tous les pixels allumés		

Figure 23: Illustration of the different hexagonal configurations

6.5.2 Stitching

The stitching functionality is intended to combine multiple images to form a larger image. This feature is particularly useful in applications where a broader field of view is necessary. As of now, the stitching functionality is not yet operational: development and testing are still ongoing. Figure [24] shows how we are supposed to have a rectangular display as in Figure [15] for example, but instead the stitching process return a square image. The problem is maybe due to the overlap on the two images stitched, or even the tilt.

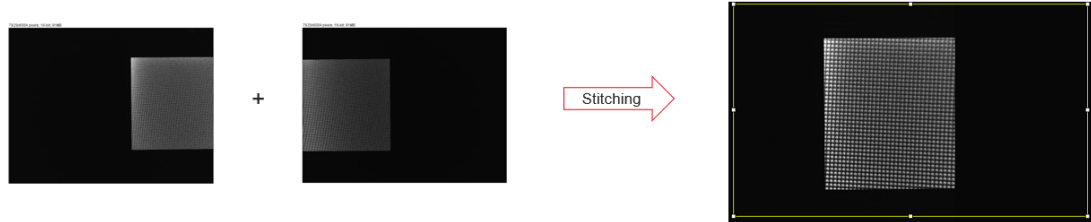


Figure 24: Illustration of the stitching function

Conclusion

This three-year apprenticeship has enabled me to develop an automated characterization system for microLEDs while significantly enhancing my technical skills in Python programming (including

object-oriented programming and human-machine interface development), radiometry, photometry, metrology and image analysis. For future enhancements, several key areas could be further improved.

One major challenge lies in automating the defect detection thresholding process. Currently, the process relies on seven manually adjusted parameters, which can be time-consuming. Implementing an adaptive optimization algorithm (such as machine learning-based system) could reduce manual intervention. Additionally, some hardware validation tests remain incomplete due to time constraints. Advanced features like hexagonal pixel processing and image stitching also warrant further development. These functionalities, once fully integrated, would enhance the system's versatility for emerging applications in photonic communications.

References

- [1] Sultan El Badaoui et al. “Data Communication Using Blue GaN-on-Si Micro-LEDs Reported on a 200-mm Silicon Substrate”. In: *IEEE Photonics Technology Letters* 36.18 (2024), pp. 1149–1152. DOI: [10.1109/LPT.2024.3451244](https://doi.org/10.1109/LPT.2024.3451244).
- [2] Mylène Sauty. “Study of the impact of alloy disorder on the electronic and optical properties of nitride semiconductor compounds and of their heterostructures.” Theses. Institut Polytechnique de Paris, June 2022. URL: <https://theses.hal.science/tel-04094691>.
- [3] François Olivier. “Étude des caractéristiques électro-optiques de micro-LED GaN pour application aux micro-écrans haute-luminance”. French. Micro et nanotechnologies / Microélectronique. PhD thesis. Université Grenoble Alpes, 2018. URL: <https://theses.hal.science/tel-01868252>.
- [4] Beatrice Wannous. “Fabrication of semipolar GaN-based μ LEDs on SOI substrates”. English. Micro and nanotechnologies/Microelectronics. PhD thesis. Université Grenoble Alpes, 2023. URL: <https://theses.hal.science/tel-04541757>.
- [5] Francois Olivier et al. “Shockley-Read-Hall and Auger non-radiative recombination in GaN based LEDs: A size effect study”. In: *Applied Physics Letters* 111.2 (July 2017), p. 022104. ISSN: 0003-6951. DOI: [10.1063/1.4993741](https://doi.org/10.1063/1.4993741). eprint: https://pubs.aip.org/aip/apl/article-pdf/doi/10.1063/1.4993741/14502019/022104__1__online.pdf. URL: <https://doi.org/10.1063/1.4993741>.
- [6] H. W. Choi et al. “Mechanism of enhanced light output efficiency in InGaN-based microlight emitting diodes”. In: *Journal of Applied Physics* 93.10 (May 2003), pp. 5978–5982. ISSN: 0021-8979. DOI: [10.1063/1.1567803](https://doi.org/10.1063/1.1567803). eprint: https://pubs.aip.org/aip/jap/article-pdf/93/10/5978/18933050/5978__1__online.pdf. URL: <https://doi.org/10.1063/1.1567803>.
- [7] Simon Litschgi et al. “Study of carrier diffusion in InGaN/GaN quantum wells: Impact of quantum well thickness and substrate type”. In: *Applied Physics Letters* 126.1 (2025), p. 011107. DOI: [10.1063/5.0219902](https://doi.org/10.1063/5.0219902).
- [8] F. Olivier et al. “Influence of size-reduction on the performances of GaN-based micro-LEDs for display application”. In: *Journal of Luminescence* 191 (2017), pp. 112–116. DOI: [10.1016/j.jlumin.2016.09.052](https://doi.org/10.1016/j.jlumin.2016.09.052). URL: <https://doi.org/10.1016/j.jlumin.2016.09.052>.